J. Fluid Mech. (2008), *vol.* 594, *pp.* 157–181.
doi:10.1017/S0022112007008877 Printed in the United Kingdom

Steady periodic waves in a three-layer fluid with shear in the middle layer

MICHAEL J. CHEN AND LAWRENCE K. FORBES

School of Mathematics and Physics, University of Tasmania, Hobart, Australia 7001

(Received 22 March 2007 and in revised form 3 September 2007)

A three-layer intrusion flow is considered, in which all three layers are in motion, with different speeds, relative to the observer. Shear is present in the middle layer, and the lowest fluid may even move oppositely to the upper two (so giving an exchange flow). Two thin interfaces are present, above and below the moving middle layer. A linearized analysis is presented for small wave amplitudes. Nonlinear periodic solutions are then obtained using a Fourier technique, and reveal a range of nonlinear phenomena, including limiting waves, multiple solutions and resonances.

1. Introduction

The propagation of steady periodic waves in layered fluids is a well-documented phenomenon. Such a situation may arise when the continuous density profile of an ocean or atmosphere has been approximated to one made up of multiple horizontal layers of constant density. Typically systems of two or three layers are considered, usually under the influence of gravity, with interest lying principally in the shape of the interfacial wave profile(s).

Previous models have varied in complexity with the inclusion of a range of effects and approximations. A simple case is that of Saffman & Yuen (1982) who considered steady finite amplitude periodic waves on a vortex sheet. Their work proposes the existence of limiting cases (such as Stokes' corners and overhanging waves as later computed by Meiron & Saffman 1983 and Turner & Vanden-Broeck 1986) as well as making a distinction between the existence of steady solutions and their stability. Another two-layer flow is that considered by Pullin & Grimshaw (1983) which included constant vorticity and a rigid lid in the upper layer. This Boussinesq flow displays an impressive range of geometrically limiting cases, which alter markedly as a physical parameter such as upper layer depth is varied.

More recently some equally interesting results have been published for the case of three-layer fluids. Although this is a natural extension, it is complicated somewhat by the presence of two interfaces. Such situations have been characterized as possessing free-surface waves which may induce or interact with internal interfacial waves (Părău & Dias 2001). Michallet & Dias (1999) have considered waves in three-layer systems that contain rigid horizontal walls above the uppermost fluid and below the lowermost one. Their focus was on the interaction between long- and short-wavelength modes of solutions. Similar effects were studied in nearly identical situations by both Rusås & Grue (2002) and Vanden-Broeck & Turner (1992). These latter authors included a middle layer of continuously varying density, and computed long waves with oscillatory tails.

The experimental work done on these types of flows is instructive. Sutherland, Kyba & Flynn (2004) looked at an intrusive gravity current propagating in a two-layer fluid. This was extended to account for more complex stratification by Flynn & Sutherland (2004), who included a lower layer of variable density. Further work by Mehta, Sutherland & Kyba (2002) on intrusions into two and three-layer fluids of constant density emphasizes the generation of solitary wave type phenomena. These studies illustrate the variety of practical contexts to which these intrusion flows apply, and confirm the relevance of the theoretical calculations of the type presented here.

The present work extends that of Forbes, Hocking & Farrow (2006), which dealt with periodic waves on an intrusion layer flowing into a stationary fluid. In that paper, the simplification of only allowing the central layer to be in motion permitted limiting waves (with sharp corners at the crests) to be computed, while resonant interactions were unavailable (or at least not found in their numerical results). Solitary wave-type solutions are also permitted for this configuration, and were obtained by Forbes & Hocking (2007) using both weakly nonlinear theory and direct numerical calculation. The computation of generalized solitary waves on fluid interfaces is a rich field of research. Akylas & Grimshaw (1992) obtained solitary waves with oscillatory tails, for instance, while Rusås & Grue (2002) have computed extreme overhanging solitary waves in a three-layer fluid. The effect of linear density stratification in each layer on the propagation of solitary waves has been examined by Fructus & Grue (2004).

The three-layer model presented here is a straightforward one. Each layer is of constant density, and is inviscid and incompressible. Shear (constant vorticity) is present in the middle layer, with the two outer layers flowing (when unperturbed) at a constant speed, such that velocity is continuous at the two interfaces. Historically, interest in systems of this type has been with regard to their stability to small perturbations. Lamb (1932, article 232) reported on the solution obtained by Rayleigh, for the stability of an intrusion 'jet'. This linearized analysis was summarized and extended by Forbes *et al.* (2006). A stability analysis of the present problem was first given by Taylor (1931). Chandrasekhar (1961) repeated this analysis with the slight simplification of only considering small density differences between the layers. The stability of the waves will not be considered here, however, with the focus instead being on computing the shape of the interfaces in steady flow. As discussed by Saffman & Yuen (1982) and Turner & Vanden-Broeck (1986), it is legitimate to make a distinction between the existence of finite amplitude steady periodic solutions and their stability. Techniques developed by Forbes *et al.* (2006) to compute periodic nonlinear interface shapes for the related problem of intrusion currents will be adapted to the present situation. Problems of this type (and shear flows in particular) have previously yielded wave profiles with overhanging portions (for instance, Turner & Vanden-Broeck 1986; Pullin & Grimshaw 1983) and the numerical scheme will be extended to account for this possibility.

The flow we consider here is physically relevant to a number of geophysical situations. For instance in Williams, Jenkins & Determann (1998) the circulation generated beneath melting ice sheets and the subsequent interaction of fresh and salt water gives rise to a type of intrusive current. In a similar fashion the agricultural run-off or inflow into a stratified reservoir may produce an intrusion flow when it reaches its neutral buoyancy: see, for example, Forbes *et al.* (2006). The outflow of water from the Mediterranean sea into the North Atlantic, as outlined in Candela (2001), and the associated phenomenon of 'meddies' is a larger-scale example of this

kind of flow. Here patches of circulating warm salty water contribute significantly to variations in salinity as they drift around the region.

In this paper, the model is formulated in such a way that it is possible to specify that the upper and lower layers flow in opposite directions, giving a so-called exchange flow. Such flows occur in a wide range of situations, for instance in the strait of Gibraltar, as discussed by Timmermans & Pratt (2005). They are also studied from a hydraulic perspective (e.g. Armi & Farmer 1986) with view to finding some maximal flow rate solution.

It has been seen in work on similar problems, such as that of Părău & Dias (2001) and Rusås & Grue (2002), that for a given choice of physical parameters there may be small amplitude solutions available at multiple wavelengths for the same wave speed. In such cases it may be possible, in a nonlinear regime, to obtain resonant interactions between these solution modes where their respective wavelengths are near-integer multiples. Interactions of this type are not dissimilar to Wilton's ripples (Wilton 1915), which are encountered for periodic gravity waves with surface tension, or the gravity-capillary waves of Chen & Saffman (1980), where various resonances (or 'combination waves') were excited as a surface tension parameter was varied. Such waves have been seen experimentally by Mehta *et al.* (2002) for the case of a bulbous intrusion into a stationary layered fluid. In this work it will be seen that superharmonic resonant interactions are readily available and coincide with complicated relationships between various physical parameters. These types of resonances are often characterized as an interaction between internal and external modes (Lewis, Lake & Ko 1974; Părău & Dias 2001), although this is not necessarily an accurate interpretation here.

The model will be derived in § 2. A linearized solution is presented in § 3, hinting at the possibility of resonant effects and multiple solutions. Section 4 introduces a numerical solution method based on Fourier series and a simple Galerkin technique. A multitude of nonlinear solutions for moderate to large amplitude waves is shown in § 5. These are compared to the linearized solution and reveal a wide array of nonlinear phenomena.

2. Model and governing equations

We consider a system composed of three horizontal fluid layers, all of which are in motion, as illustrated in figure 1. Throughout this paper the top layer will be denoted as layer 1, the middle as layer 2 and the lowest as layer 3. Each fluid layer has constant density ρ_i, $i = 1, 2, 3$, with $\rho_1 < \rho_2 < \rho_3$, and there are constant horizontal background flow speeds c_1 and c_3 in the top and bottom layers, respectively. There are two free interfaces, $y = \eta_U$ and $y = \eta_L$, at the upper and lower boundaries of the middle layer. The upper and lower layers are unbounded, of infinite vertical extent. Constant vorticity (shear) is present in the middle layer, where the background speed is such that it matches the outer layer speeds in the case of flat interface profiles. All fluids are assumed to be incompressible and inviscid. The upper and lower layers are also assumed to flow irrotationally. The flow is steady and subject to the downward acceleration g of gravity. The shape of the two interfaces will be of particular interest.

Non-dimensional variables will be introduced. The height of the middle layer, h, is used as a length scale. A typical speed, $\sqrt{gh}$, is chosen as the velocity scale with velocity potentials scaled with $h\sqrt{gh}$. The density scale is ρ_2, the density of the middle

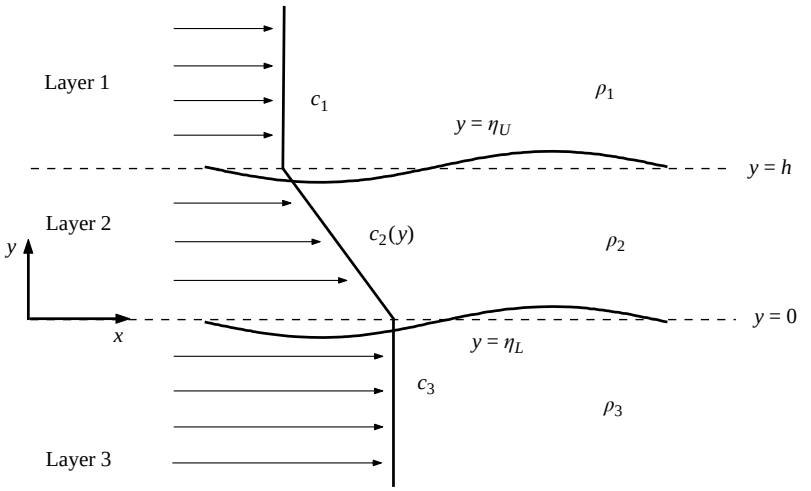

FIGURE 1. Diagram of the flow configuration showing the three fluid layers moving horizontally with waves propagating at the two interfaces $y = \eta_U$ and $y = \eta_L$ above and below the middle layer.

layer. Recasting the problem in these terms, the system is characterized by four dimensionless parameters:

$$F_1 = \frac{c_1}{\sqrt{gh}}, \quad F_3 = \frac{c_3}{\sqrt{gh}}, \tag{2.1}$$

$$D_1 = \frac{\rho_1}{\rho_2}, \quad D_3 = \frac{\rho_3}{\rho_2}. \tag{2.2}$$

Here F_1 and F_3 are Froude numbers for the upper and lower layers respectively. These are the fluid celerities made dimensionless with respect to the characteristic speed $\sqrt{gh}$ of a wave in the middle layer. The two remaining parameters D_1 and D_3 are density ratios relative to the density ρ_2 of the middle layer, with $D_1 < 1$ and $D_3 > 1$. The appropriate form of the background speed in the middle layer is

$$F_2(y) = F_3 + (F_1 - F_3)y. \tag{2.3}$$

Here the linear dependence on y represents the constant shear. The fluid speed in this layer matches those of the upper and lower layers on the planes $y = 1$ and $y = 0$, respectively.

In each layer we define a velocity vector $\boldsymbol{q}_i = u_i \boldsymbol{i} + v_i \boldsymbol{j}$ $(i = 1, 2, 3)$. For the two outer layers $\boldsymbol{q}_i$ is the gradient of a velocity potential ϕ_i,

$$\begin{aligned} \phi_i &= F_i x + \Phi_i \\ \boldsymbol{q}_i &= \left(F_i + \frac{\partial \Phi_i}{\partial x} \right) \boldsymbol{i} + \frac{\partial \Phi_i}{\partial y} \boldsymbol{j} \quad (i = 1, 3). \end{aligned} \tag{2.4}$$

The velocity vector in the middle layer, $\boldsymbol{q}_2$, may be expressed in a similar fashion:

$$\boldsymbol{q}_2 = \left(F_3 + (F_1 - F_3)y + \frac{\partial \Phi_2}{\partial x} \right) \boldsymbol{i} + \frac{\partial \Phi_2}{\partial y} \boldsymbol{j}. \tag{2.5}$$

Here we have effectively written the velocity as the sum of a rotational part (the linear shear term) and an irrotational part (gradient of the velocity potential Φ_2). Having

done this we may also determine the streamfunction in the middle layer,

$$\psi_2(x, y) = F_3 y + \frac{1}{2}(F_1 - F_3)y^2 + \Psi_2(x, y) \tag{2.6}$$

where the irrotational part of the streamfunction, Ψ_2, is related to irrotational velocity potential Φ_2 by the Cauchy–Riemann equations.

Conservation of mass requires that ϕ_1, Φ_2 and ϕ_3 satisfy Laplace's equation in each fluid layer:

$$\nabla^2\phi_1 = 0 \quad \text{in } \eta_u < y < \infty, \tag{2.7}$$

$$\nabla^2\Phi_2 = 0 \quad \text{in } \eta_L < y < \eta_U, \tag{2.8}$$

$$\nabla^2\phi_3 = 0 \quad \text{in } -\infty < y < \eta_L. \tag{2.9}$$

It is of note that the shape of these layers is determined by the shape of the two interfaces (not known *a priori*), making this a highly nonlinear problem.

There are several boundary conditions which need to be defined on each interface. Two kinematic conditions on the upper interface require that neither the upper nor middle fluid layers may cross the interface:

$$v_i = u_i \frac{\partial \eta_U}{\partial x} \quad (i = 1, 2). \tag{2.10}$$

A single dynamic condition,

$$\begin{aligned} &\tfrac{1}{2}D_1F_1^2 - \tfrac{1}{2}D_1\left(u_1^2 + v_1^2\right) - D_1(\eta_U - 1) \\ &\quad = \tfrac{1}{2}F_3^2 - \tfrac{1}{2}\left(u_2^2 + v_2^2\right) + (F_1 - F_3)\psi_2 - (\eta_U - 1), \end{aligned} \tag{2.11}$$

is obtained (via Bernoulli's equation) by equating pressure in each layer at the interface.

Similarly, there are two kinematic conditions on the lower interface,

$$v_i = u_i \frac{\partial \eta_L}{\partial x} \quad (i = 2, 3), \tag{2.12}$$

for each of the lower and middle layers. The dynamic condition on the lower interface is

$$\tfrac{1}{2}F_3^2 - \tfrac{1}{2}\left(u_2^2 + v_2^2\right) + (F_1 - F_3)\psi_2 - \eta_L = \tfrac{1}{2}D_3F_3^2 - \tfrac{1}{2}D_3\left(u_3^2 + v_3^2\right) - D_3\eta_L. \tag{2.13}$$

The infinite vertical extent of the upper and lower fluids requires that

$$\begin{aligned} \phi_1 &\to F_1 x \quad \text{as} \quad y \to +\infty, \\ \phi_3 &\to F_3 x \quad \text{as} \quad y \to -\infty, \end{aligned} \tag{2.14}$$

for a solution to be physically reasonable. Our interest lies in investigating the nature of periodic waves on the interfaces. As such we seek periodic solutions in x for ϕ_1, Φ_2, ϕ_3, η_U and η_L, which satisfy equations (2.7)–(2.14). To this end we assume that the system is also dependent on some dimensionless wavenumber, k, which is thus an additional dimensionless parameter, along with the Froude numbers (2.1) and density ratios (2.2), needed to specify a solution completely.

3. Linearized solution

We now present a linearized solution to the governing equations (2.7)–(2.14). This corresponds to the case of the two free surface shapes being sinusoidal in x and of

small amplitude. In effect we use a small perturbation about the trivial solution of flat interfaces and background flow for the velocity in each fluid layer, similar to that presented by Taylor (1931) but without the time dependence. The velocity potentials in (2.7)–(2.9) are expressed by means of the perturbed expansions

$$\phi_1(x, y) = F_1 x + \epsilon \Phi_{11}(x, y) + \mathcal{O}(\epsilon^2), \tag{3.1}$$

$$\Phi_2(x, y) = \epsilon \Phi_{21}(x, y) + \mathcal{O}(\epsilon^2), \tag{3.2}$$

$$\phi_3(x, y) = F_3 x + \epsilon \Phi_{31}(x, y) + \mathcal{O}(\epsilon^2), \tag{3.3}$$

while the lower and upper interface profiles are perturbations about $y = 0$ and $y = 1$ respectively:

$$\eta_L(x) = \epsilon H_{L1}(x) + \mathcal{O}(\epsilon^2), \tag{3.4}$$

$$\eta_U(x) = 1 + \epsilon H_{U1}(x) + \mathcal{O}(\epsilon^2). \tag{3.5}$$

Here ϵ is a small parameter with magnitude in the order of the amplitude of the wave. Appropriate solutions to Laplace's equation are chosen for each velocity potential, up to a multiplicative constant:

$$\Phi_{11}(x, y) = a_{11} \mathrm{e}^{-k(y-1)} \sin kx, \tag{3.6}$$

$$\Phi_{31}(x, y) = a_{31} \mathrm{e}^{ky} \sin kx, \tag{3.7}$$

$$\Phi_{21}(x, y) = (c_2 \cosh(ky) + d_2 \sinh(ky)) \sin kx. \tag{3.8}$$

These have been chosen to have period $2\pi/k$ in x, to be odd with respect to x and to have the properties that Φ_{11} and Φ_{31} decay to zero as $y \to \infty$ and $y \to -\infty$, respectively. The perturbed streamfunction (2.6) in the middle layer, ψ_2, takes the linearized form

$$\psi_2(x, y) = F_3 y + \frac{1}{2}(F_1 - F_3) y^2 + \epsilon \Psi_{21}(x, y) + \mathcal{O}(\epsilon^2), \tag{3.9}$$

in which Ψ_{21} is determined from the Cauchy–Riemann equations to be

$$\Psi_{21}(x, y) = (c_2 \sinh(ky) + d_2 \cosh(ky)) \cos kx. \tag{3.10}$$

The corresponding interface profiles will be periodic, even functions in x, and will have the forms

$$H_{L1}(x) = \cos kx, \quad H_{U1}(x) = \alpha \cos kx, \tag{3.11}$$

where α is to be determined. Substituting this perturbed solution into the boundary conditions (2.10)–(2.13) and then discarding any terms of order ϵ^2 or higher, we obtain a system of six algebraic equations. These may be solved to yield the dispersion relation

$$\mathscr{D}_1 k F_3^2 + \mathscr{D}_3 k F_1^2 + \mathscr{D}_1 \mathscr{D}_3 \tanh k + k^2 F_1^2 F_3^2 \tanh k = 0, \tag{3.12}$$

where

$$\mathscr{D}_1 = D_1 k F_1^2 - F_1(F_1 - F_3) - (1 - D_1),$$

and

$$\mathscr{D}_3 = D_3 k F_3^2 + F_3(F_1 - F_3) - (D_3 - 1).$$

This relation determines the co-dependency of the Froude numbers on wavenumber such that equations (2.7)–(2.14) are satisfied to first order in the parameter ϵ.

Equation (3.12) contains cubic powers of the Froude numbers, suggesting that up to three linear solutions may exist for some fixed wavenumber. Likewise the expression involves nonlinear functions of wavenumber k, which indicates that, for fixed Froude numbers (2.1) and density ratios (2.2), there may be multiple linear solutions of different wavenumber. It is impractical to try to characterize completely the effect of varying each of the five non-dimensional parameters, so the density ratios, D_1 and D_3, will be held constant at values close to 1 (representative of stratified oceans or reservoirs), and the upper-layer Froude number will be chosen as $F_1 = 0.1$, throughout the results presented here.

3.1. *The linearized dispersion relation*

Although the dispersion relation (3.12) must ultimately be solved numerically to determine the relationship between wavenumber k and Froude number F_3, it is instructive to consider first a limiting case. For short wavelengths (that is, large wavenumber, k) we put $\tanh k \approx 1$ to reduce (3.12) to a simple cubic in F_3. This may be solved exactly to give the three approximate values

$$F_3 \approx \frac{1 - D_1 + F_1^2(1 - k - kD_1)}{F_1}, \tag{3.13}$$

and

$$F_3 \approx \frac{-F_1 \pm \sqrt{F_1^2 + 4(1 - k - D_3 + kD_3^2)}}{2(kD_3 + k - 1)}, \tag{3.14}$$

for the speed F_3 of the lowest fluid layer. The first of these, (3.13), takes the opposite sign to F_1 (for large enough k), suggesting that the lower layer may flow in the opposite direction to the upper layer; this is therefore an 'exchange flow'. The two solutions in equation (3.14) have slower speeds in the bottom layer, and typical parameter values give one positive and one negative value for F_3.

A numerical solution to (3.12) is required for small and moderate values of k. This is obtained by holding D_1, D_3 and F_1 constant, choosing a value for k and then solving for F_3 with Newton's method. This was repeated over a range of initial values of F_3 that were chosen to allow for multiple solutions at the same wavenumber. Having done this we may compare the relative amplitude and phase of the two linearized interfaces in equation (3.12) by taking

$$\begin{aligned}\alpha = \frac{H_{U1}}{H_{L1}} = \frac{1}{(1 - D_1)kF_3}[&kF_1(\mathscr{D}_3 \cosh k + kF_3^2 \sinh k)\\ &+ (D_1 kF_1 - (F_1 - F_3))(kF_3^2 \cosh k + \mathscr{D}_3 \sinh k)],\end{aligned} \tag{3.15}$$

which will be negative if the interfaces are out of phase and positive if they are in phase. The ratio α goes to infinity as F_3 passes through zero, simply indicating a flat lower interface at this point.

An example solution is shown in figure 2. Physically reasonable parameter values have been chosen with $D_1 = 0.99$, $D_3 = 1/D_1$ and $F_1 = 0.1$. These values have been taken to be representative of typical situations encountered in oceanography: see Phillips (1969). In the diagram, in-phase solutions are represented by solid lines with out of phase solutions represented by dashed lines. For this example we see three distinct solution branches: an in-phase solution for all k with positive F_3; an out-of-phase solution available for $k > \kappa_2$ with two negative F_3 values at each wavenumber; and a solution valid for $k < \kappa_1$ that emerges, out of phase, from $k = 0$ with positive Froude number, switches phase as it passes through $F_3 = 0$ and then

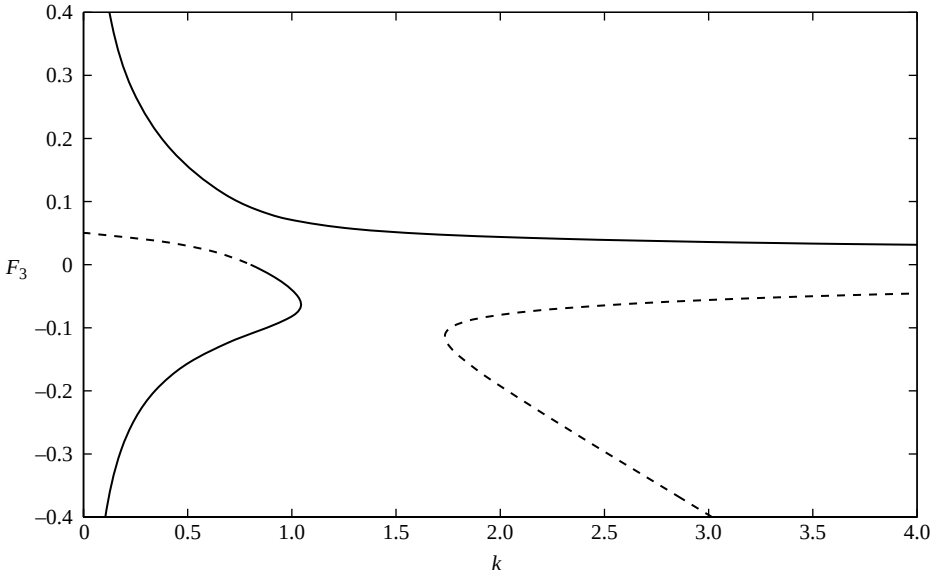

FIGURE 2. Plot of the linearized dispersion relation (3.12) to give the relationship between wavenumber k and lower-layer Froude number F_3. The parameter values chosen are upper-layer Froude number $F_1 = 0.1$ and density ratios $D_1 = 0.99$ and $D_3 = 1/0.99$.

has long-wavelength solutions for increasingly strongly negative F_3. Here, the values κ_1 and κ_2 represent wavenumbers at which the linearized solution branches in figure 2 have turning points, with vertical slopes. Two additional points of interest on this final branch are the Froude number where $k = 0$,

$$F_{30} = \frac{(1 - D_1)(D_3 - 1)}{F_1(D_3 - D_1)} = 5.025 \times 10^{-2}, \tag{3.16}$$

possibly corresponding to a solitary wave-like solution, and the wavenumber, κ_0, for $F_3 = 0$, which from equation (3.12) satisfies

$$\kappa_0 F_1^2 + [\kappa_0 F_1^2 D_1 - F_1^2 - (1 - D_1)] \tanh \kappa_0 = 0 \tag{3.17}$$

and may be easily found numerically (in this case $\kappa_0 = 0.8022$). Similarly we may calculate the turning points κ_1 and κ_2 by taking the derivative of equation (3.12) with respect to F_3, giving, in this case, $\kappa_1 = 1.044$ and $\kappa_2 = 1.735$.

It can be seen that two solutions exist (one in-phase and one out-of-phase) for lower layer Froude number less than the value F_{30} of equation (3.16). Where the wavenumbers of two such solutions are integer multiples of each other there is the possibility of resonant behaviour, with solutions from the two branches superposed. Previous studies (e.g. Părău & Dias 2001) have found that in a nonlinear regime such resonances are readily excited for moderate to large amplitude nonlinear waves, since at a fixed wavenumber, the Froude number may vary (from its linearized value) as amplitude increases, allowing nearby resonances to be encountered. The likelihood of a particular resonance being available for a value of F_3 may be evaluated with the aid of figure 3. Here the ratio of the short and long wavenumbers has been plotted against F_3. It can be seen that this ratio becomes large for strongly negative F_3, as well as where $F_3 \to F_{30}$ and $F_3 \to 0$. The dotted horizontal lines indicate where

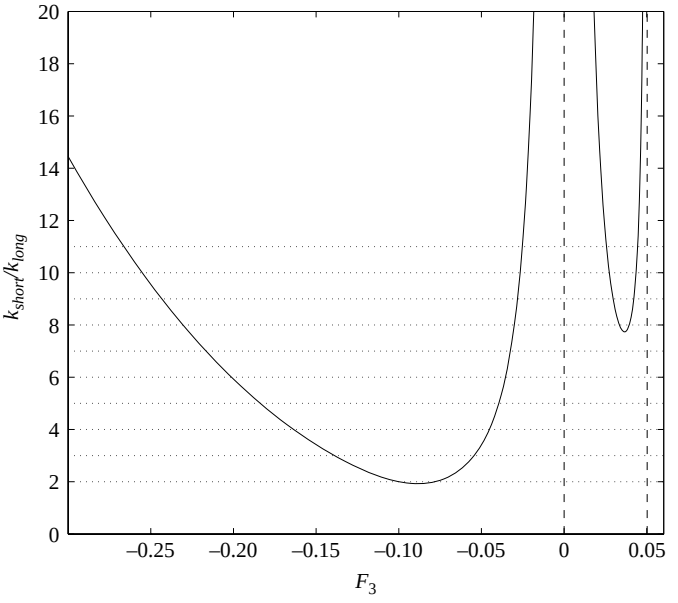

FIGURE 3. Plot of the ratio of wavenumbers when two linearized solutions exist for the same lower-layer Froude number. The lower-layer Froude number F_3 is shown on the horizontal axis. Linear resonance is possible where the ratio is integer-valued.

the ratio is integer valued. It may be seen that, for instance, linear theory predicts 1:2-type resonances near $F_3 \approx -0.08$.

4. Nonlinear solutions and numerical scheme

We will now outline a numerical procedure to obtain periodic solutions to the (fully nonlinear) equations (2.7)–(2.14). This is essentially a Galerkin-type method used to determine the coefficients of some Fourier series. There is a possibility that the interfacial profiles may become multivalued (as in Pullin & Grimshaw 1983 and Rusås & Grue 2002) and a reparametrization of the system involving arclength will be introduced to deal with this possibility.

Appropriate solutions to Laplace's equations (2.7)–(2.9) (subject to (2.14)) will be Fourier series of the form

$$\Phi_1 = \sum_{n=1}^{N} B_n \mathrm{e}^{-nk(y-1)} \sin nkx, \tag{4.1}$$

$$\Phi_2 = \sum_{n=1}^{N} [C_n \cosh nk(y-1/2) + D_n \sinh nk(y-1/2)] \sin nkx, \tag{4.2}$$

$$\Phi_3 = \sum_{n=1}^{N} F_n \mathrm{e}^{nky} \sin nkx, \tag{4.3}$$

with these approximate solutions becoming exact as $N \to \infty$. It is occasionally convenient numerically to replace the hyperbolic functions in Φ_2 with simple exponential functions.

It is convenient to parametrize each interface using an arclength s, so that each interface is represented in the form $(x(s), y(s))$. A change of variables will now be made with a scaled arclength, ξ, defined as

$$\xi = \frac{2\pi s}{L}.$$

Here, L is the total arclength along one wave cycle; this is therefore a parameter which is essentially equivalent to a measure of amplitude and need not be computed explicitly. The use of an arclength leads to an extra condition which must be satisfied on each interface, namely

$$\left(\frac{\mathrm{d}x}{\mathrm{d}\xi}\right)^2_{U,L} + \left(\frac{\mathrm{d}y}{\mathrm{d}\xi}\right)^2_{U,L} = \frac{L^2_{U,L}}{4\pi^2}, \tag{4.4}$$

where the subscripts U and L refer to the upper and lower profiles, respectively. This is derived from the usual Pythagorean relationship $\mathrm{d}x^2 + \mathrm{d}y^2 = \mathrm{d}s^2$. The periodic functions representing the upper interface $(x, y) = (x_U, \eta_U)$ and the lower interface $(x, y) = (x_L, \eta_L)$ are selected to be Fourier series of the form

$$\eta_U = 1 + P_0 + \sum_{n=1}^{N} P_n \cos n\xi, \tag{4.5}$$

$$\eta_L = R_0 + \sum_{n=1}^{N} R_n \cos n\xi, \tag{4.6}$$

$$x_U = \frac{\xi}{k} + \sum_{n=1}^{N} T_n \sin n\xi, \tag{4.7}$$

$$x_L = \frac{\xi}{k} + \sum_{n=1}^{N} U_n \sin n\xi, \tag{4.8}$$

which also become exact as $N \to \infty$.

As we seek finite amplitude nonlinear wave solutions for the interface profiles, it is necessary to define some measure of wave amplitude. Half the peak-to-trough displacement of the lower interface, $\mathscr{A}_L$, is chosen here, and may be calculated from

$$2\mathscr{A}_L = \eta_L(0) - \eta_L(\pi). \tag{4.9}$$

This adds an extra parameter to this system, as well as an extra condition which must be satisfied by our solution. Where the upper interface is of much larger amplitude, its displacement may be used instead of equation (4.9) to define the amplitude parameter.

A nonlinear solution is characterized by the $8N + 3$ coefficients from the velocity potentials (the B_n, C_n, D_n and F_n), the coefficients from the interface profile coordinates (the P_n, R_n, T_n and U_n) and the lower layer Froude number, F_3. The numerical scheme involves forming a vector of unknowns, $\boldsymbol{V}$, from these coefficients,

$$\boldsymbol{V} = [\boldsymbol{B}; \boldsymbol{C}; \boldsymbol{D}; \boldsymbol{F}; \boldsymbol{P}; \boldsymbol{R}; \boldsymbol{T}; \boldsymbol{U}; P_0; R_0; F_3]^T,$$

where $\boldsymbol{B} = [B_1, \ldots, B_n]$, $\boldsymbol{C} = [C_1, \ldots, C_n]$ and so on, and then iteratively solving for the components of this vector with a Newton's method routine in $8N + 3$ dimensions, seeking to minimize an error vector $\boldsymbol{E}$. The first $8N$ components of the error are calculated by successively multiplying (2.10)–(2.13) and (4.4) by a Fourier basis function (N times for each equation) and integrating over one period. The remaining

three sets of components come from the two dynamic conditions (2.11) and (2.13) integrated over a period and the wave amplitude condition. Explicitly, the components of the error vector $\boldsymbol{E}$ are derived from the two upper interface kinematic conditions (2.10) on $(x, y) = (x_U, \eta_U)$,

$$\int_{-\pi}^{\pi} \left(v_1 \frac{\partial x_U}{\partial \xi} - u_1 \frac{\partial \eta_U}{\partial \xi} \right) \sin j\xi \, \mathrm{d}\xi = 0, \tag{4.10}$$

$$\int_{-\pi}^{\pi} \left(v_2 \frac{\partial x_U}{\partial \xi} - u_2 \frac{\partial \eta_U}{\partial \xi} \right) \sin j\xi \, \mathrm{d}\xi = 0, \tag{4.11}$$

for $j = 1, \ldots, N$, suitably decomposed and integrated. Similarly, from the lower interface kinematic conditions (2.12), evaluated on $(x, y) = (x_L, \eta_L)$, we obtain

$$\int_{-\pi}^{\pi} \left(v_2 \frac{\partial x_L}{\partial \xi} - u_2 \frac{\partial \eta_L}{\partial \xi} \right) \sin j\xi \, \mathrm{d}\xi = 0, \tag{4.12}$$

$$\int_{-\pi}^{\pi} \left(v_3 \frac{\partial x_L}{\partial \xi} - u_3 \frac{\partial \eta_L}{\partial \xi} \right) \sin j\xi \, \mathrm{d}\xi = 0, \tag{4.13}$$

for $j = 1, \ldots, N$. The upper dynamic condition (2.11) is first integrated to give one error component,

$$\int_{-\pi}^{\pi} \Big[\tfrac{1}{2} F_3^2 - \tfrac{1}{2} D_1 F_1^2 - \tfrac{1}{2}(u_2^2 + v_2^2) + \tfrac{1}{2} D_1 (u_1^2 + v_1^2) + (F_1 - F_3)\psi_2 - (1 - D_1)(\eta_U - 1) \Big] \mathrm{d}\xi = 0, \tag{4.14}$$

and then multiplied by the even basis functions $\cos j\xi$ to give a further N error components

$$\int_{-\pi}^{\pi} \Big[\tfrac{1}{2} F_3^2 - \tfrac{1}{2} D_1 F_1^2 - \tfrac{1}{2}(u_2^2 + v_2^2) + \tfrac{1}{2} D_1 (u_1^2 + v_1^2) + (F_1 - F_3)\psi_2 - (1 - D_1)(\eta_U - 1) \Big] \cos j\xi \, \mathrm{d}\xi = 0, \tag{4.15}$$

for $j = 1, \ldots, N$. Likewise, another $N + 1$ components are obtained by applying the same procedure to the lower dynamic condition (2.13),

$$\int_{-\pi}^{\pi} \Big[\tfrac{1}{2}(1 - D_3) F_3^2 - \tfrac{1}{2}(u_2^2 + v_2^2) + \tfrac{1}{2} D_3 (u_3^2 + v_3^2) + (F_1 - F_3)\psi_2 - (1 - D_3)\eta_L \Big] \mathrm{d}\xi = 0, \tag{4.16}$$

$$\int_{-\pi}^{\pi} \Big[\tfrac{1}{2}(1 - D_3) F_3^2 - \tfrac{1}{2}(u_2^2 + v_2^2) + \tfrac{1}{2} D_3 (u_3^2 + v_3^2) + (F_1 - F_3)\psi_2 - (1 - D_3)\eta_L \Big] \cos j\xi \, \mathrm{d}\xi = 0, \tag{4.17}$$

for $j = 1, \ldots, N$. Finally, multiplying the two arclength conditions (4.4) by the even Fourier basis functions and integrating provides a further $2N$ components of the error

vector,

$$\int_{-\pi}^{\pi} \left[\left(\frac{\partial x_U}{\partial \xi} \right)^2 + \left(\frac{\partial \eta_U}{\partial \xi} \right)^2 \right] \cos j\xi \, \mathrm{d}\xi = 0, \tag{4.18}$$

$$\int_{-\pi}^{\pi} \left[\left(\frac{\partial x_L}{\partial \xi} \right)^2 + \left(\frac{\partial \eta_L}{\partial \xi} \right)^2 \right] \cos j\xi \, \mathrm{d}\xi = 0, \tag{4.19}$$

for $j = 1, \ldots, N$. The last component of the error vector comes from the wave amplitude condition (4.9) on the lower interface,

$$\sum_{n=1}^{N} R_n [1 - \cos n\pi] - 2\mathscr{A}_L = 0, \tag{4.20}$$

which has been derived using the Fourier series (4.6).

All integrals in equations (4.10)–(4.19) are evaluated using a simple trapezoidal rule over a grid with equal point spacing, since this is exponentially accurate for periodic integrands: see Atkinson (1978, p. 253). To this end the interface profiles (and then their associated derivatives) are computed at each of the grid points, and these profiles are used to compute the velocities and streamfunctions on the two free surfaces. All these are used, in turn, to calculate the components of the error vector. It is required that sufficiently many grid points are used for the integrals to be evaluated accurately; success was achieved using about $16N$ grid points. The number of coefficients used in the series, N, was chosen to be at most 201. It was found that $N = 51$ performed well, with 801 grid points used in the integration.

This numerical scheme is sensitive to the absolute size of the velocity potential coefficients B_n, C_n, D_n and F_n. In particular, the hyperbolic functions in the middle layer potential are susceptible to becoming very large, which in turn affects the convergence of the Newton's method routine. Such ill-conditioning may be avoided by rewriting each coefficient in a new scaled form,

$$B_n = B_n^* \exp(nk(\beta - 1)) \tag{4.21}$$

$$\begin{bmatrix} C_n \\ D_n \end{bmatrix} = \begin{bmatrix} C_n^* \\ D_n^* \end{bmatrix} \frac{1}{\cosh nk(\delta - 1/2)} \tag{4.22}$$

$$F_n = F_n^* \exp(-nk\gamma), \tag{4.23}$$

with these replacing the original coefficients in the vector of unknowns. For small amplitude waves it is satisfactory for the scaling parameters β, γ and δ to be set to zero. As the amplitude of the waves increases these values may be increased.

To improve the rate of convergence in the Newton's method scheme the initial guess of a previously calculated solution of a smaller amplitude was used, that is, $\boldsymbol{V}_{i_{init}} = \boldsymbol{V}_{i-1_{final}}$. This was further improved (on occasion) by using a scaled linear interpolation based on two previous solutions of smaller amplitude with the initial guess

$$\boldsymbol{V}_{i_{init}} = \boldsymbol{V}_{i-1_{final}} + (\boldsymbol{V}_{i-1_{final}} - \boldsymbol{V}_{i-2_{final}}) \frac{\mathscr{A}_i - \mathscr{A}_{i-1}}{\mathscr{A}_{i-1} - \mathscr{A}_{i-2}},$$

although this is only of use where the relationship between Froude number and amplitude varies monotonically.

The Newton's method routine involves calculating a Jacobian matrix of first derivatives at each iteration, $\boldsymbol{J} = \left[\partial E_i / \partial V_j\right]$. For longer-wavelength cases and

moderate amplitudes it was sufficient to calculate this matrix using a simple forward difference routine. However, shorter-wavelength solutions were found to be more sensitive to the choice of scaling parameters and it was difficult to calculate limiting solutions when the approximate Jacobian was used. In such cases the exact Jacobian was used, and this also saw a slight increase in the efficiency of the routine.

5. Results

The numerical scheme outlined in § 4 was run extensively. For each set of nonlinear solutions the wavenumber was fixed and the lower-layer Froude number allowed to vary with amplitude. Throughout, the density ratios were fixed at the same values $D_1 = 0.99$ and $D_3 = 1/0.99$ illustrated in figure 2, for the linearized solution of § 3. From figure 2 it may be seen that there are two regions of wavelength where three linearized solutions of different lower Froude number exist. This was of consideration in selecting the nonlinear solutions to compute, with a wavelength from each chosen for further investigation. Firstly, a long-wavelength case (with two in-phase solutions and one out-of-phase solution) at $k = 0.5$ was selected and, secondly, a shorter wavelength case at $k = 2.5$ (with two out-of-phase solutions and one in-phase solution) was also chosen. In each of these six cases the linearized solution agrees very well with the computed small-amplitude nonlinear solutions. Unless otherwise stated all solutions have been computed with $N = 51$, which was found to be a sufficient number of coefficients to evaluate the interfacial profiles reliably.

It will be seen that many of the following results involve a delicate relationship between F_3 and amplitude, in which two solutions occur for nearly indistinguishable values of those parameters. These fine features were obtained by first calculating solutions using fewer coefficients (typically $N = 31$), for which such features are much coarser, and less accurate. This lower-coefficient solution is then used as an initial guess in Newton's method to obtain results for solutions of successively more coefficients (up to the desired $N = 51$) which would otherwise be extremely difficult to compute from other starting guesses. As a check, results in a number of cases have been run with as many as $N = 101$ Fourier coefficients; this is computationally demanding, but does not significantly affect the results, confirming that the results with $N = 51$ coefficients have already converged to a good degree of accuracy.

5.1. *Results for* $k = 0.5$

The first solution we will consider is the in-phase wave with positive lower-layer Froude number. The linearized solution predicts that at small amplitudes $F_3 = 0.1556$ with the amplitudes of the two interfaces in the ratio $\alpha = H_{U1}/H_{L1} = 1.3177$. The nonlinear solution is shown in figure 4(*a*) as a solid curve, and the linearized result is drawn with a dashed line. The two are in very close agreement for small amplitude. However, as the nonlinear $(\mathscr{A}_L, F_3)$ curve is followed, a more complicated situation arises.

At first, lower-layer Froude number increases with amplitude up to a maximum of $\mathscr{A}_L \approx 0.6$. This maximum corresponds to a solution for which there are two slightly square sinusoids of similar amplitude on the two interfaces. From this maximum both amplitude and lower-layer Froude number decrease, backtracking along the $(\mathscr{A}_L, F_3)$ curve very closely, before diverging away from this at moderate amplitudes. The solutions along this portion of the curve appear, initially, to approach the configuration of a triangle wave on the upper interface and a moderate amplitude sinusoid on the lower interface. However, near the solution at $(\mathscr{A}_L, F_3) \approx (0.1, 0.24)$

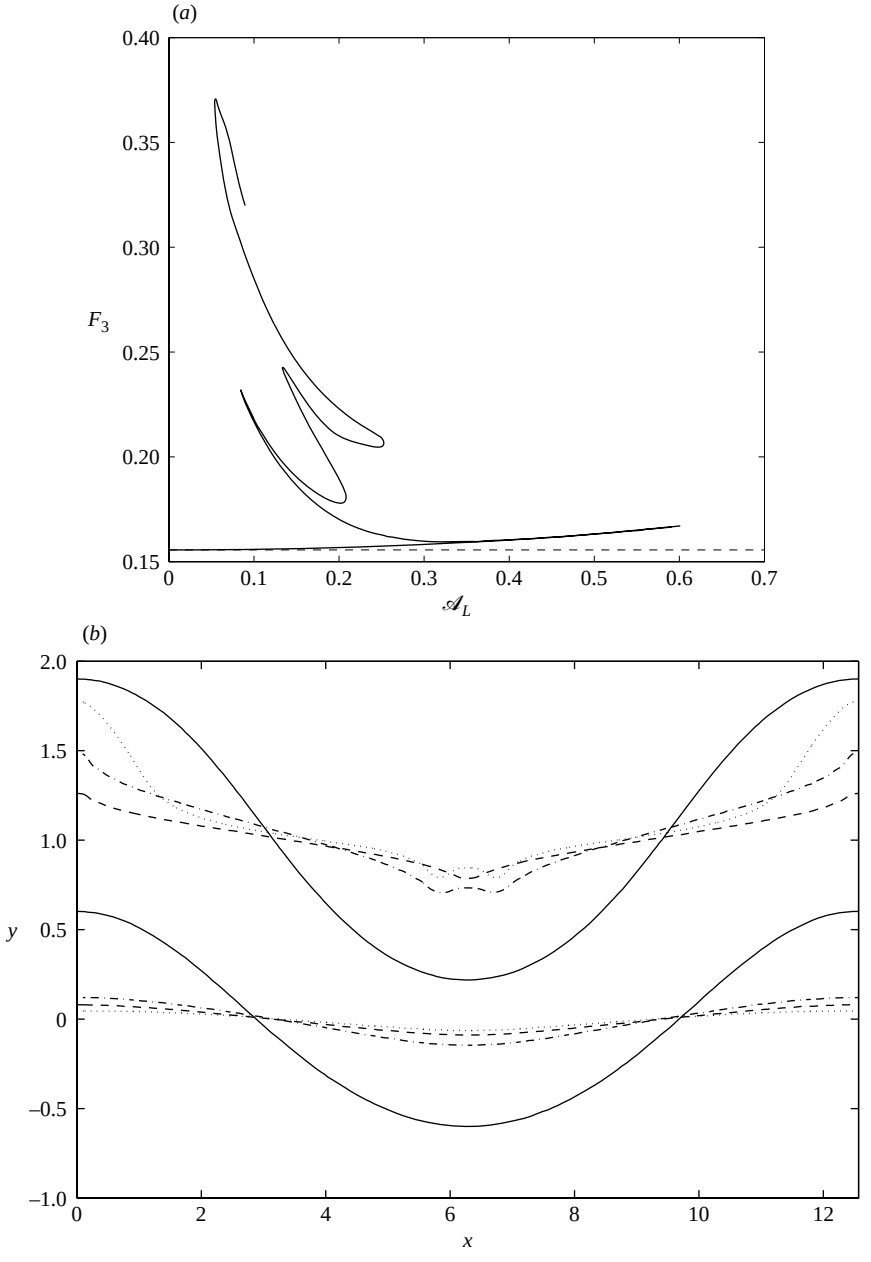

FIGURE 4. (*a*) Dependence of Froude number F_3 on lower-wave amplitude $\mathscr{A}_L$ for $k = 0.5$, the in-phase case with positive Froude number. (*b*) Four interfacial profiles for the in-phase case with positive Froude number at $k = 0.5$. The solutions shown are $(\mathscr{A}_L, F_3) = (0.601, 0.167)$ (solid lines), $(\mathscr{A}_L, F_3) = (0.0844, 0.232)$ (dashed lines), $(\mathscr{A}_L, F_3) = (0.133, 0.243)$ (dotted lines) and $(\mathscr{A}_L, F_3) = (0.0547, 0.371)$ (dash-dot lines).

the upper interface develops a small lump at its trough, a feature that is maintained as these solutions are followed in $(\mathscr{A}_L, F_3)$ space.

The interfacial profiles associated with the solutions from the first four of the peak-like artifacts on the amplitude–Froude number curve are shown in figure 4(*b*).

The largest of these, drawn with solid lines, represents a solution for $(\mathscr{A}_L, F_3) = (0.601, 0.167)$. The dashed lines are the solution for $(\mathscr{A}_L, F_3) = (0.0844, 0.232)$, the profiles for $(\mathscr{A}_L, F_3) = (0.133, 0.243)$ are illustrated with dotted lines while the dash-dot lines represent the highest Froude number solution at $(\mathscr{A}_L, F_3) = (0.0547, 0.371)$. In the last three of these solutions a dimple-like lump can be seen at the trough of the upper interface. In addition, for the highest Froude number case a steep bump at the crest of the upper interface has evolved. A bump of this type also appears in the last solutions obtained before the numerical method diverged, and may possibly indicate the incipient formation of a limiting structure such as an overhanging 'mushroom' near the crest.

The linearized solution for the out-of-phase branch at this wavelength predicts that $F_3 = 0.02986$, with $\alpha = -2.3013$, shown in figure 5(*a*) as a horizontal dotted line. Again, the nonlinear solution (the solid and dashed lines in figure 5(*a*), with the amplitude $\mathscr{A}_U$ of the upper interface being used for convenience) is in close agreement with this for small amplitudes, but starts to decrease as amplitude is increased. Here the $(\mathscr{A}_U, F_3)$ curve is made up of a series of disjointed sets of solutions shown alternatively in solid and dashed lines for clarity. Each of these curves contains a section that traces out part of a decrease in lower-layer Froude number for increasing amplitude. This acts as a kind of lower bound in $(\mathscr{A}_U, F_3)$ space, with the convoluted $(\mathscr{A}_U, F_3)$ curves which bifurcate off from the branch never crossing below it. In this region both interfacial profiles are nearly sinusoidal.

Above this lower bound the various $(\mathscr{A}_U, F_3)$ curves are quite convoluted, with the two variables related in a highly nonlinear fashion. Here the lower interfacial profiles are distinguished by the presence of a superposed wave of shorter wavelength $2\pi/nk$, where n is an integer, on top of the primary wave of wavelength $2\pi/k$. These are a kind of superharmonic (1:n) resonance with the secondary mode of solutions which are allowed at the same Froude number. This is confirmed by the fact that the tangled nonlinear branches in figure 5(*a*) bifurcate from the lower branch at four resonance values. Two of these resonant branches have been traced right back to their intersection with the $\mathscr{A}_U$ axis, showing that there are at least three solutions of infinitesimal upper-interface amplitude, only one of which is a linearized solution. At both these points the lower interface is of moderate amplitude.

Three of these superharmonic type solutions have been tracked exhaustively (the 1:9, 1:10 and 1:11 cases) and some example wave profiles are shown in figures 5(*b*)–(*d*). Two 1:9 resonance solutions of identical Froude number are plotted in figure 5(*b*); here the solid lines are interfacial profiles for $(\mathscr{A}_U, F_3) = (0.0644, 0.310)$ while the dashed lines are solutions for $(\mathscr{A}_U, F_3) = (0.0629, 0.310)$. Figure 5(*c*) shows two 1:10 resonance solutions, again of similar Froude number, with the solid lines being the solutions for $(\mathscr{A}_U, F_3) = (0.104, 0.303)$ and the dashed lines the profiles for $(\mathscr{A}_U, F_3) = (0.0946, 0.303)$. The final class of superharmonic solutions which were able to be computed accurately were 1:11 resonances. The solid lines are the waves profiles for $(\mathscr{A}_U, F_3) = (0.109, 0.300)$, while the dashed lines are profiles for $(\mathscr{A}_U, F_3) = (0.0980, 0.300)$. In each of these cases the shorter-wavelength component may be superposed either in or out of phase with the primary wave. This corresponds to the two curves which leave the main branch in figure 5(*a*) at each of the superharmonic resonance bifurcations. As a consequence each of the disjoint curves in the $(\mathscr{A}_U, F_3)$-space may contain two types of superharmonic solution. For instance, the first dotted line in figure 5(*a*) begins with an out-of-phase 1:9-type solution, progresses until the short-wavelength component disappears with an in-phase 1:10 resonance being excited at a slightly larger amplitude.

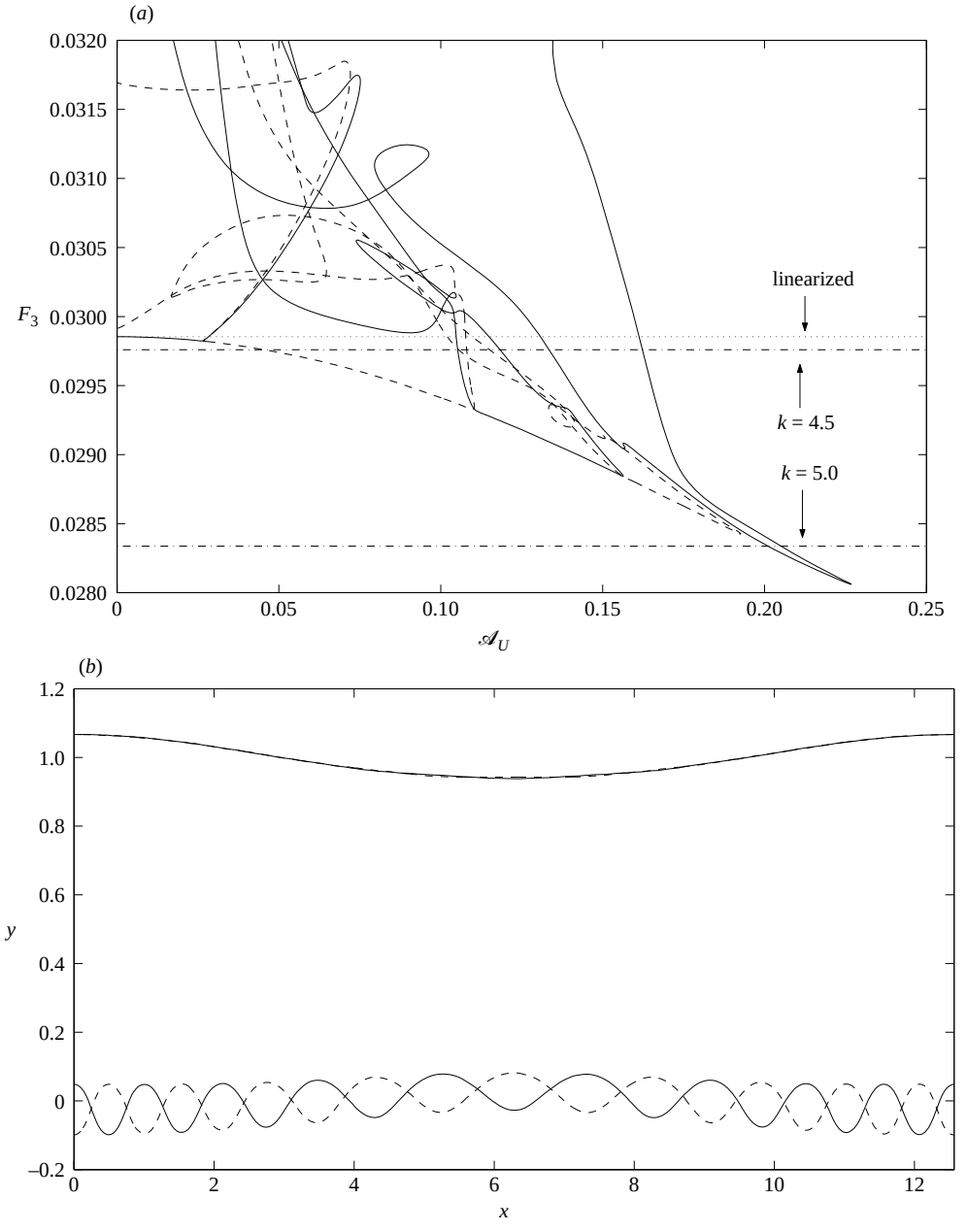

FIGURE 5(a, b). For caption see facing page.

The linearized solutions for $9k = 4.5$ and $10k = 5$ near the appropriate Froude number are shown in figure 5(a) as horizontal dash-dot lines. It may be seen that in each case the superharmonic is excited at a larger Froude number than linear theory suggests is possible. Indeed it appears that the larger the amplitude of the primary wave, the further from the linearized solution a superharmonic is first available.

The third linearized solution at this wavelength is an in-phase exchange flow with $F_3 = -0.1567$ and $\alpha = 0.7555$, shown with the horizontal dotted line in figure 6(a).

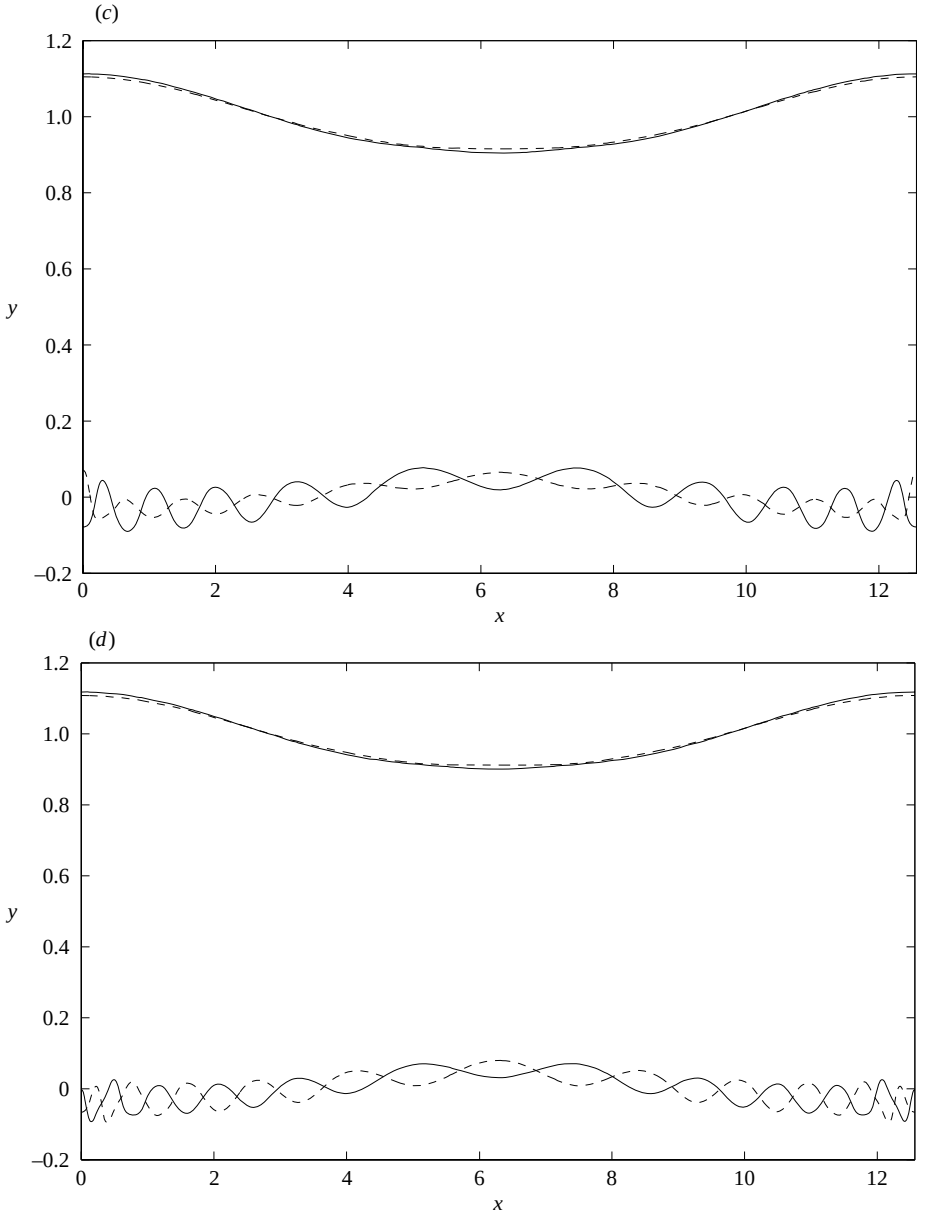

FIGURE 5. (*a*) Dependence of Froude number F_3 on upper-wave amplitude $\mathscr{A}_U$ for $k = 0.5$, the out-of-phase case with positive Froude number. (*b*) Two interfacial profiles for the 1:9 resonance at equal lower-layer Froude number. The short-wavelength mode is out of phase with the primary wave for the solution at $(\mathscr{A}_U, F_3) = (0.0644, 0.310)$ (solid lines) and in phase for the solution at $(\mathscr{A}_U, F_3) = (0.0629, 0.310)$ (dashed lines). (*c*) Two interfacial profiles for the 1:10 resonance at equal lower-layer Froude number. The short-wavelength mode is in phase with the primary wave for the solution at $(\mathscr{A}_U, F_3) = (0.104, 0.303)$ (solid lines) and out of phase for the solution at $(\mathscr{A}_U, F_3) = (0.0946, 0.303)$ (dashed lines). (*d*) Two interfacial profiles for the 1:11 resonance at equal Froude number. The short-wavelength mode is out of phase with the primary wave for the solution at $(\mathscr{A}_U, F_3) = (0.109, 0.300)$ (solid lines) and in phase for the solution at $(\mathscr{A}_U, F_3) = (0.0980, 0.300)$ (dashed lines).

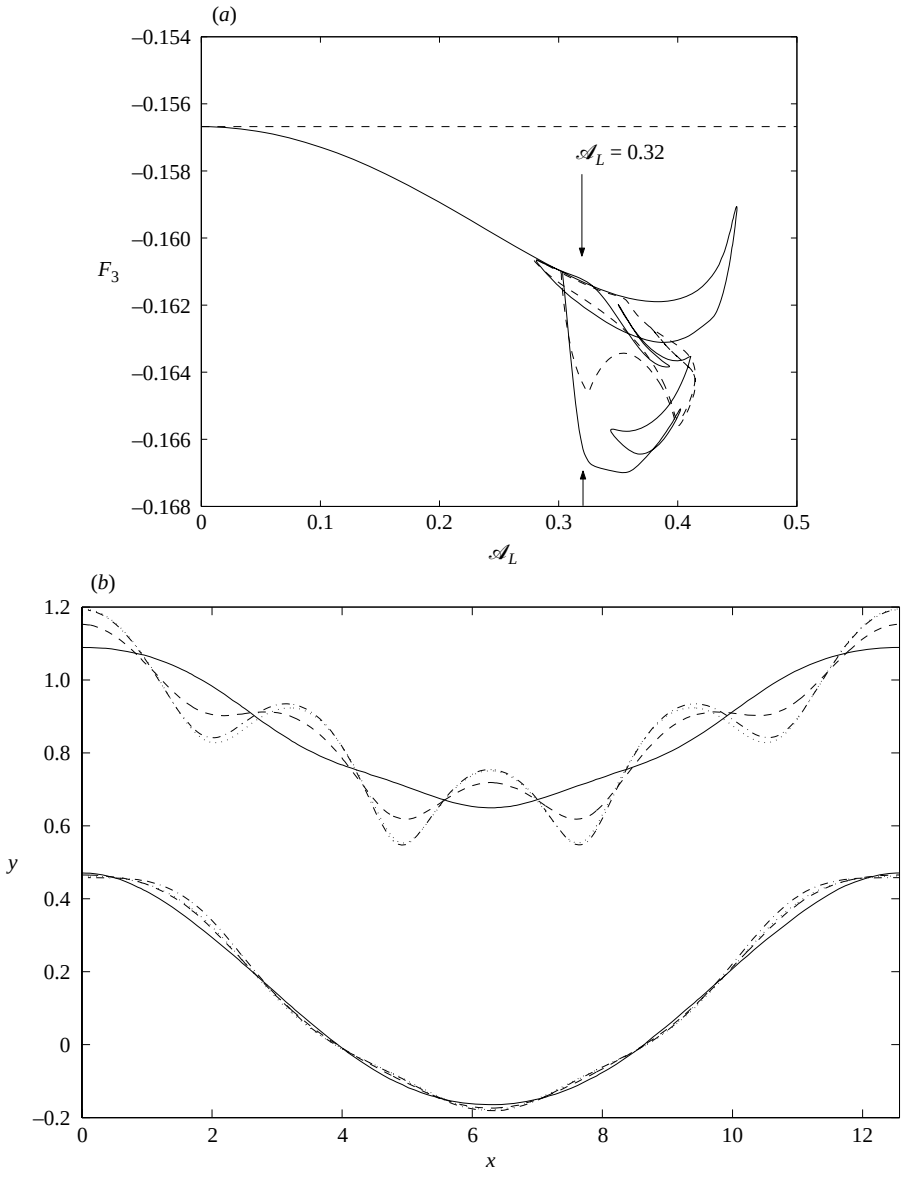

FIGURE 6(a, b). For caption see facing page.

Again the nonlinear solution (the solid and dashed lines in figure 6a) is found to be in strong agreement for small amplitudes. As amplitude is increased, Froude number F_3 becomes more strongly negative, with the two interfaces taking a slightly pointed nonlinear wave shape, the lower profile having a larger amplitude than the upper.

At a moderate amplitude, about $\mathscr{A}_L = 0.3$, a 1:4 resonant interaction is excited and Froude number begins to increase. Here the secondary wave is larger on the upper interface and out of phase with the primary wave. As the ($\mathscr{A}_L$, F_3) curve (the solid line in figure 6a) is followed, the secondary wave becomes of moderate amplitude itself. Some solutions of this type are shown in figure 6(b), with the superposed wave itself clearly having a nonlinear shape with sharp troughs. The four wave profiles

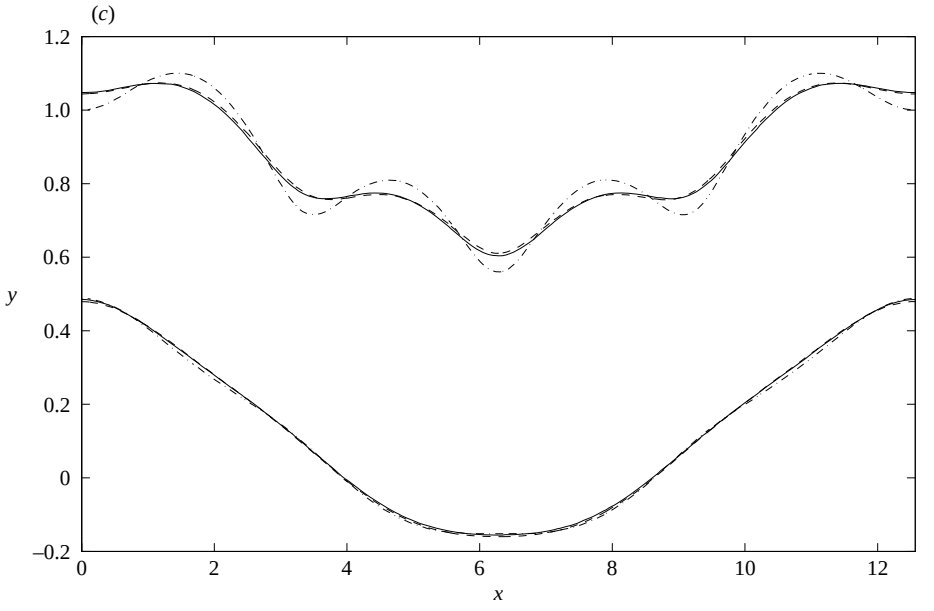

FIGURE 6. (*a*) Dependence of Froude number F_3 on lower-wave amplitude $\mathscr{A}_L$ for $k = 0.5$, the in-phase case with negative Froude number. (*b*) Four interfacial profiles for $\mathscr{A}_L = 0.32$ with a 1:4 resonance in phase with the primary solution mode. The profiles shown are for $(\mathscr{A}_L, F_3) = (0.32, -0.1614)$ (solid lines), $(\mathscr{A}_L, F_3) = (0.32, -0.1620)$ (dashed lines), $(\mathscr{A}_L, F_3) = (0.32, -0.1612)$ (dash-dot lines) and $(\mathscr{A}_L, F_3) = (0.32, -0.1662)$ (dotted lines). (*c*) Three interfacial profiles for $\mathscr{A}_L = 0.32$ with a 1:4 resonance out of phase with the primary solution mode. The profiles shown are for $(\mathscr{A}_L, F_3) = (0.32, -0.1643)$ (solid lines), $(\mathscr{A}_L, F_3) = (0.32, -0.1617)$ (dashed lines) and $(\mathscr{A}_L, F_3) = (0.32, -0.1613)$ (dash-dot lines).

in figure 6(*b*) are all of amplitude $\mathscr{A}_L = 0.32$, with the solid lines corresponding to the profiles at $(\mathscr{A}_L, F_3) = (0.32, -0.1614)$, the dashed lines being the profiles for $(\mathscr{A}_L, F_3) = (0.32, -0.1620)$, the solution at $(\mathscr{A}_L, F_3) = (0.32, -0.1612)$ being represented by the dash-dot lines, and the dotted lines are the waves' profiles for $(\mathscr{A}_L, F_3) = (0.32, -0.1662)$.

The class of solution with an in-phase secondary wave is not as readily available here as in the previous case. For these to be computed an initial guess in Newton's method was created, somewhat artificially, by taking an out-of-phase solution and multiplying the coefficients $B_4, C_4, D_4, \ldots$ by -1. Having done this the solutions of the type shown in figure 6(*c*) were obtained, with the secondary wave of opposite phase to the solutions of figure 6(*b*). These were tracked for some distance in the parameter space, as seen in the dotted line on the $(\mathscr{A}_L, F_3)$ diagram in figure 6(*a*). Three interfacial profiles are shown in figure 6(*c*) with solid lines corresponding to the solution at $(\mathscr{A}_L, F_3) = (0.32, -0.1643)$; the dashed lines are the solutions for $(\mathscr{A}_L, F_3) = (0.32, -0.1617)$ and the dash-dot lines represent the profiles for $(\mathscr{A}_L, F_3) = (0.32, -0.1613)$.

It may be seen that up to 12 distinct solutions may be obtained for some values of $\mathscr{A}_L$, such as in the highly tangled region near $A_L = 0.375$. A slightly simpler situation is represented by the seven simultaneous solutions available at the same value $\mathscr{A}_L = 0.32$ of the amplitude, as shown in figures 6(*b*) and 6(*c*). The complexity of the solution space is further emphasized by noting that the proximity of two solutions on the $(\mathscr{A}_L, F_3)$ diagram is not an indication that their interfacial profiles

are qualitatively similar. Yet another feature of these cases is the many sections of the Froude number–amplitude diagram in figure 6(*a*) which run nearly parallel to each other. In terms of the interfacial profiles these correspond to a situation where the primary wave's amplitude decreases as the secondary wave's increases, or *vice versa*. The situation for the in-phase solutions near $\mathscr{A}_L = 0.4$ is an example of this. Such an occurrence seems in line with conventional thinking about the role of energy transfer between solution modes in these sorts of resonant interactions (Phillips 1974). Both classes of solutions terminate by crossing back onto a previously calculated solution (in both cases at $\mathscr{A}_L \approx 0.3$), thus forming a complicated kind of loop structure.

5.2. *Results for* $k = 2.5$

For the in-phase solution at this wavelength, linearized theory predicts $F_3 = 0.03925$ with $\alpha = 0.04768$; that is, a lower interface of much larger amplitude than the upper. The nonlinear solutions (shown as a solid line in figure 7*a*) agree well with both predictions and we see a similar situation to that of figure 4(*a*) (a longer-wavelength example from the same mode of solutions). Again, Froude number F_3 increases with amplitude, reaching a maximum at the moderate value $\mathscr{A}_L = 0.19$ of the wave amplitude. These solutions are characterized by a nearly flat upper interface and a slightly square lower interface of moderate amplitude.

The $(\mathscr{A}_L, F_3)$ curve then turns back on itself and traces out a complicated relationship featuring numerous sharp turning points. As before, the solutions near these points correspond to dimpled waves, several of which are shown in figure 7(*b*). The solution of largest amplitude $(\mathscr{A}_L, F_3) = (0.188, 0.0421)$ is shown with a solid line, two moderate amplitude solutions at $(\mathscr{A}_L, F_3) = (0.0693, 0.0594)$ and $(\mathscr{A}_L, F_3) = (0.0986, 0.0447)$ are shown with dashed and dash-dot lines, respectively. The last computed solution, at $(\mathscr{A}_L, F_3) = (0.138, 0.0537)$ and shown in figure 7(*b*) with dotted lines, represents the point at which our numerical method failed to continue the branch shown in figure 7(*a*). No geometric limitation is obvious from these results, but it is possible that some subtle structure may be formed in the interface profiles that prevents the numerical method from continuing further.

Linear theory predicts two out-of-phase solutions at this wavelength, one at $F_3 = -0.064414$ with a large lower interface ($\alpha = -0.1126$) and another at $F_3 = -0.29616$ with a large upper interface ($\alpha = -25.8476$). Both of these are shown with horizontal dashed lines in figure 8(*a*).

The solid lines in figure 8(*a*) are nonlinear solutions for $N = 51$. The two solution branches are evidently not connected in $(\mathscr{A}_U, F_3)$ parameter space. Both sets of nonlinear solutions agree well with linear theory at small amplitudes, and this predicts that the relative amplitudes of the two interfaces in each case will be quite different. Again we see monotonic variation in Froude number as amplitude is increased, up to some maximum before the $(\mathscr{A}_U, F_3)$ curves turn back on themselves and then progress in a complicated fashion.

Solutions on the curve originating from the higher-speed exchange flow are shown in figure 8(*b*). These four curves correspond to the interfacial profiles for $(\mathscr{A}_U, F_3) = (0.1388, -0.2591)$, shown with solid lines, the dashed lines are the solution for $(\mathscr{A}_U, F_3) = (0.05704, -0.07093)$, the solution for $(\mathscr{A}_U, F_3) = (0.6327, -0.1267)$ is shown by dash-dot lines and the dotted lines represent the profiles for $(\mathscr{A}_U, F_3) = (0.1053, -0.2154)$.

These solutions have upper interfaces of much larger amplitude than their lower interfaces at smaller amplitude $\mathscr{A}_U$. As the solutions are tracked, the interfaces become of comparable amplitude. In particular, the lower interface develops dimple-like

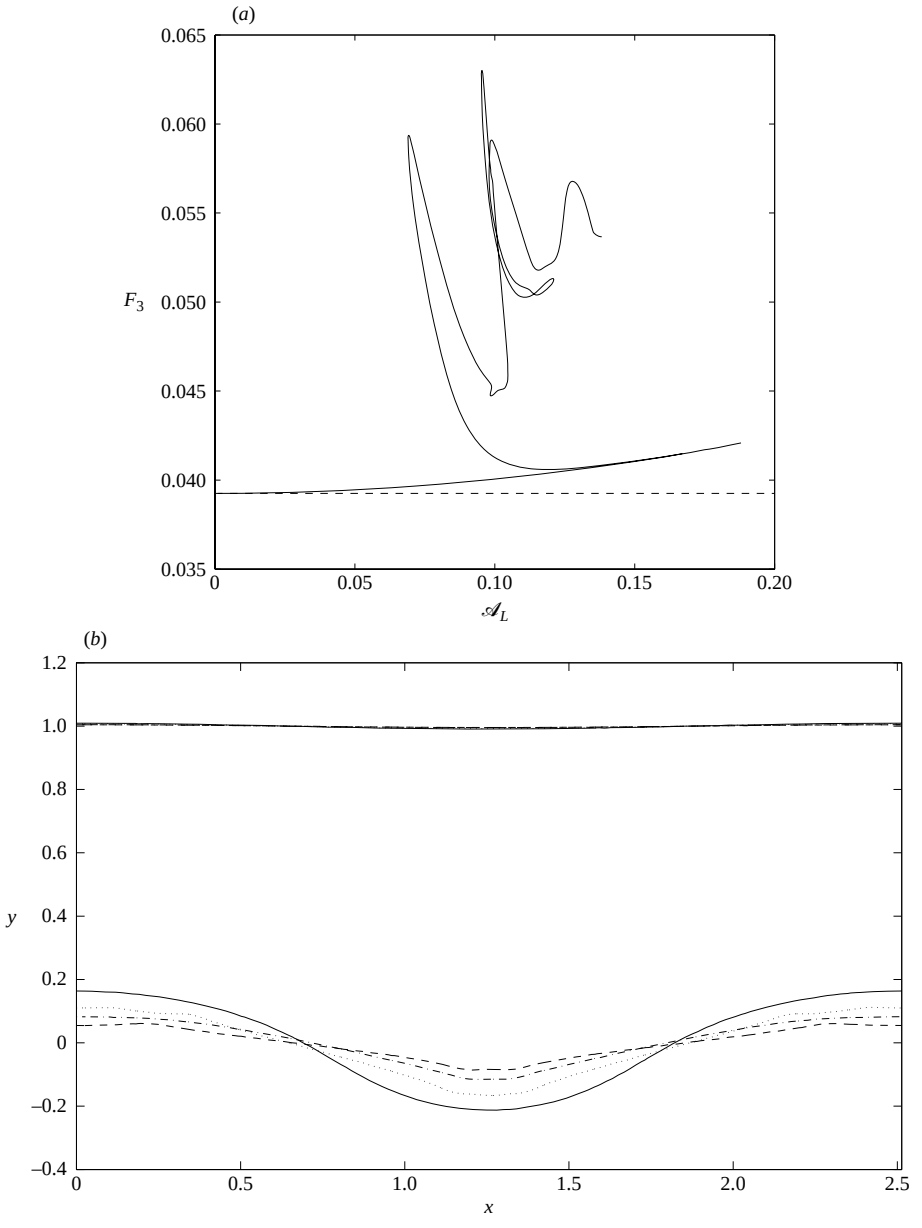

FIGURE 7. (*a*) Dependence of Froude number F_3 on lower-wave amplitude $\mathscr{A}_L$ for $k = 2.5$, the in-phase case with positive Froude number. (*b*) Four interfacial profiles for the in-phase case with positive Froude number at $k = 2.5$. The profiles shown are for $(\mathscr{A}_L, F_3) = (0.188, 0.0421)$ (solid lines), $(\mathscr{A}_L, F_3) = (0.0693, 0.0594)$ (dashed lines), $(\mathscr{A}_L, F_3) = (0.0986, 0.0447)$ (dash-dot lines) and $(\mathscr{A}_L, F_3) = (0.138, 0.0537)$ (dotted lines).

features at its trough and crest, as well as increasing in mean height. The upper interface, however, remains approximately sinusoidal. It is possible that the dotted profile for $(\mathscr{A}_U, F_3) = (0.1053, -0.2154)$ is close to a limiting solution with an overhanging structure at the crest of the lower interfacial wave, since near-vertical portions are present in the computed profile.

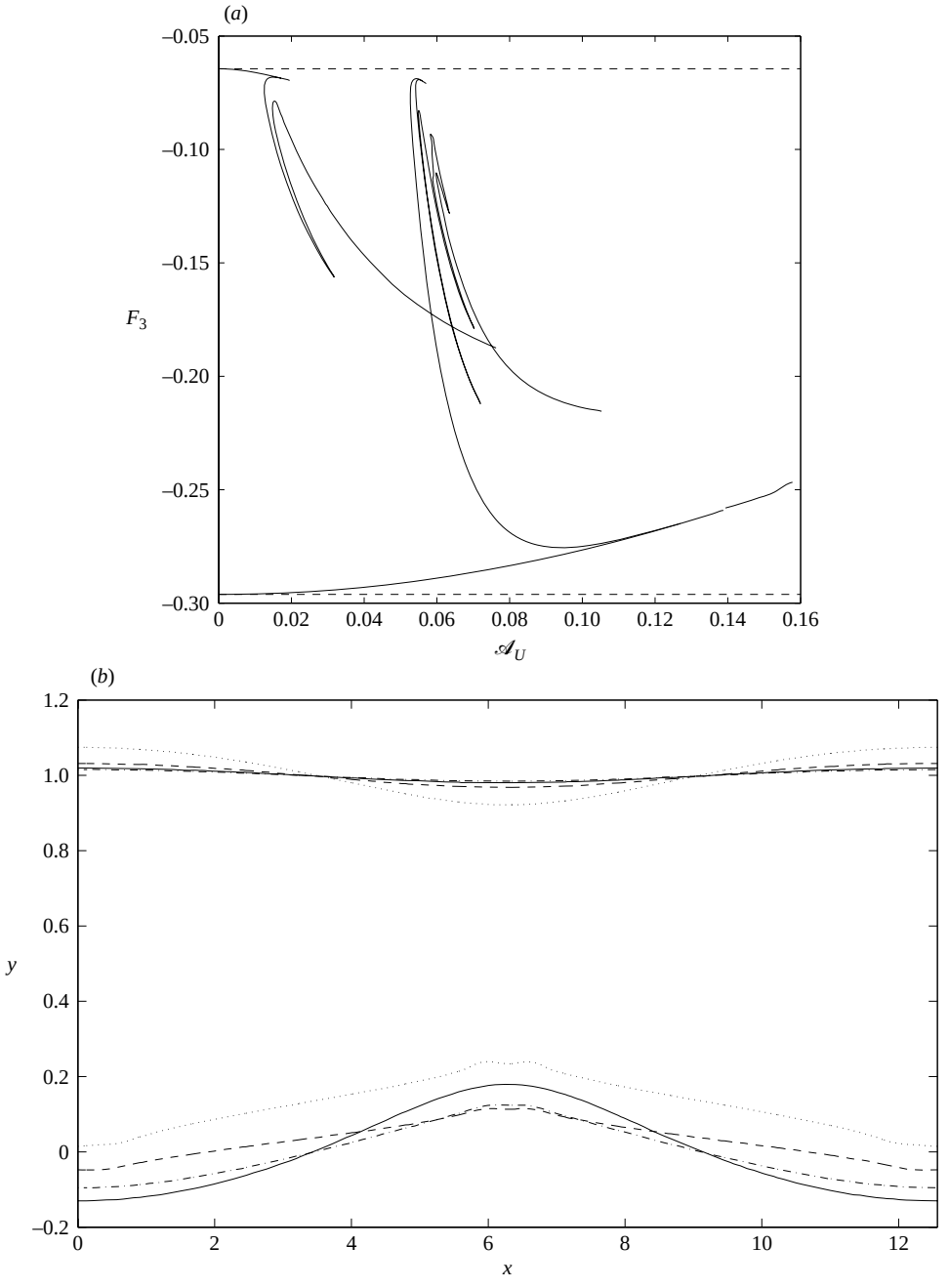

FIGURE 8(*a*, *b*). For caption see facing page.

The case originating from the slower exchange flow displays a similar pattern of behaviour. Some example solutions may be seen in figure 8(*c*). The profiles shown with solid lines are for the parameters values $(\mathscr{A}_U, F_3) = (0.01951, -0.06958)$, the dashed lines show the solution for $(\mathscr{A}_U, F_3) = (0.03172, -0.1562)$, the solution for $(\mathscr{A}_U, F_3) = (0.01534, -0.07866)$ is shown with dash-dot lines and the dotted lines are the profiles for $(\mathscr{A}_U, F_3) = (0.07627, -0.1875)$.

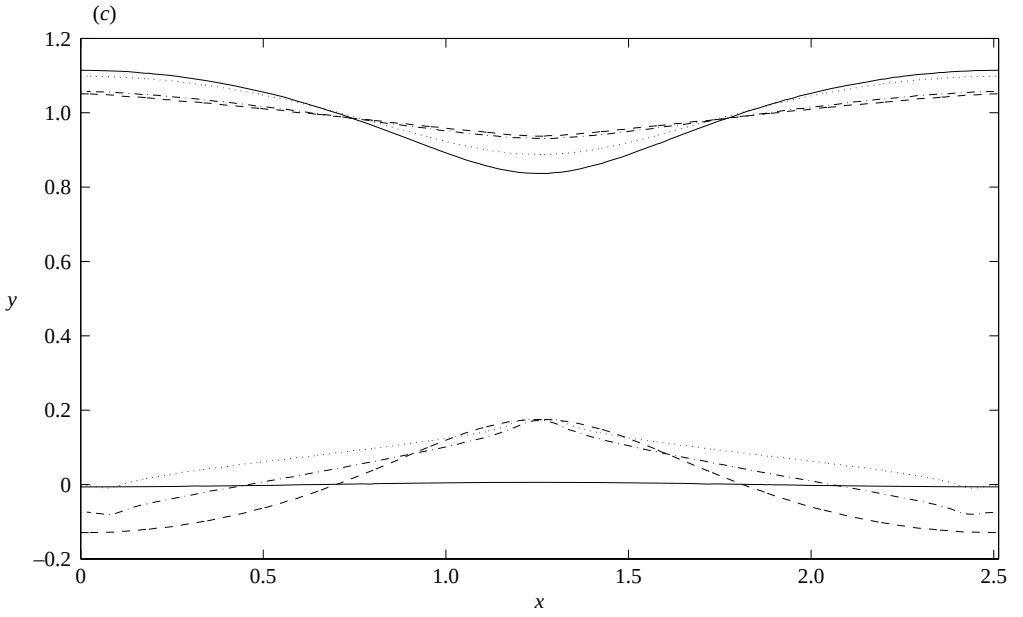

FIGURE 8. (*a*) Dependence of Froude number F_3 on upper-wave amplitude $\mathscr{A}_U$ for $k = 2.5$, both the out-of-phase cases with negative Froude number. (*b*) Four interfacial profiles originating from out-of-phase case with large negative Froude number at $k = 2.5$. The profiles shown are for $(\mathscr{A}_U, F_3) = (0.1388, -0.2591)$ (solid lines), $(\mathscr{A}_U, F_3) = (0.05704, -0.07093)$ (dashed lines), $(\mathscr{A}_U, F_3) = (0.6327, -0.1267)$ (dash-dot lines) and $(\mathscr{A}_U, F_3) = (0.1053, -0.2154)$ (dotted lines). (*c*) Four interfacial profiles originating from out-of-phase case with small negative Froude number at $k = 2.5$. The profiles shown are for $(\mathscr{A}_U, F_3) = (0.01951, -0.06958)$ (solid lines), $(\mathscr{A}_U, F_3) = (0.03172, -0.1562)$ (dashed lines), $(\mathscr{A}_U, F_3) = (0.01534, -0.07866)$ (dash-dot lines) and $(\mathscr{A}_U, F_3) = (0.07627, -0.1875)$ (dotted lines).

Here the interfacial profiles possess a larger-amplitude lower interface for small to moderate amplitudes. Past the first sharp feature on the $(\mathscr{A}_U, F_3)$ curve in figure 8(*a*) the two interfaces eventually become of similar amplitude. These solutions are qualitatively similar to those calculated for the fast exchange flow, with lumps at their peaks and troughs. Indeed, the last computed solutions from the two $(\mathscr{A}_U, F_3)$ curves closely resemble each other, both having a lower interface which displays lumps as well as a significant positive mean displacement.

Notice that there is, in fact, a second small disjoint branch of solutions in $(\mathscr{A}_U, F_3)$ parameter space just beyond $\mathscr{A}_U = 0.14$. This is shown in figure 8(*a*). It may represent a remnant of a subharmonic solution which is not able to be continued accurately numerically here beyond the small portion shown.

6. Discussion and conclusion

This paper has presented a wide array of nonlinear solutions to the problem of steady periodic waves on an intrusion layer with constant vorticity. These were seen to agree well with the predictions of linear theory for small amplitudes, with nonlinear effects leading to some highly irregular behaviour for moderate and large amplitudes. Small amplitude solutions which did not coincide with the linearized solution were also present. The numerical scheme used was a straightforward extension to that of Michallet & Dias (1999) and Forbes *et al.* (2006), with a reparametrization of the

problem using arclength to allow for the possibility of overhanging waves. Although no such waves were computed, the possibility of overhanging limiting profiles was suggested by some of the numerical results. In addition it is possible that overhanging waves might be encountered for different (and less relevant) values of the physical parameters; their absence does not reveal a limitation of the numerical technique, and in fact such solutions would be subject to Rayleigh–Taylor instability, so that interest in them is somewhat academic. In this paper, we chose density ratios close to unity to represent a stratified ocean or reservoir, whereas the dramatically overhanging solitary waves computed by Rusås & Grue (2002) were for fluid density ratios (in our notation) of $D_1 = 0.57$ and $D_3 = 1.43$. When this choice of density ratio was used in the present problem no overhanging profiles were obtained, however, suggesting that the profiles of Rusås & Grue were due (at least in part) to the presence of a horizontal wall in the bottom fluid layer.

It has been assumed here that the shear in the middle layer is exactly the amount required to make the velocity profile in the three fluids continuous, when both interfaces are horizontal. This was done to mimic the expected effects of viscosity. However, as the fluids here are inviscid, tangential slip at each interface is possible, and so equation (2.3) could be replaced with the more general sheared flow $F_2 = F_3 + \gamma y$, in which the extra parameter γ is left arbitrary. We have made some preliminary investigations of the effect of varying this parameter γ, but find no major qualitative differences with results presented here. A systematic study of the complete range of possibilities for this parameter's effect on the behaviour of solutions is beyond the scope of the present investigation and, in any event, the value of $\gamma = (F_1 - F_3)$ used here is surely of the most physical relevance.

A variety of superharmonic resonances between the different solution modes were computed in this study. In the out-of-phase case at $k = 0.5$, where successive $1:n$ resonances were computed with the shorter wavelength component either in or out of phase, this type of solution was especially abundant. It was seen that, in a nonlinear regime, these resonances were able to be excited at an earlier wave speed than linear theory predicted, with this effect becoming more pronounced for larger-amplitudes of the primary mode of solution.

The stability of the nonlinear solutions is an open question. The infinitesimal solutions of § 3 will be neutrally stable. Further investigation is required, however, to determine the precise nature of the finite amplitude solutions in a time-dependent regime. It was seen that, where resonant effects were not present, the maximum-amplitude solutions were quite weakly nonlinear and without any obvious geometric limitation. This appears to be in line with the notion of a 'dynamical limit', as suggested by Saffman & Yuen (1982), the point beyond which any larger-amplitude solutions will be unstable. Future work will include formulating a time-dependent version of this problem, possibly in a similar manner to that which the Rayleigh–Taylor instability was computed by Forbes, Chen, & Trenham (2007). Such a technique would easily permit a finite-amplitude solution computed in this paper to be used as an initial condition in a time-dependent formulation of the flow.

REFERENCES

Akylas, T. R. & Grimshaw, R. H. J. 1992 Solitary internal waves with oscillatory tails. *J. Fluid Mech.* **242**, 279–298.

Armi, L. & Farmer, D. M. 1986 Maximal two-layer exchange through a contraction with barotropic flow. *J. Fluid Mech.* **164**, 27–51.

Atkinson, K. E. 1978 *An Introduction to Numerical Analysis.* Wiley.

Candela, J. 2001 Mediterranean water and global circulation. In *Ocean Circulation and Climate* (ed. G. Siedler, J. Church & J. Gould), pp. 419–429. Academic Press.

Chandrasekhar, S. 1961 *Hydrodynamic and Hydromagnetic Stability*. Dover.

Chen, B. & Saffman, P. G. 1980 Steady gravity-capillary waves on deep water. Part II. Numerical results for finite amplitude. *Stud. Appl. Maths* **62**, 95–111.

Flynn, M. R. & Sutherland, B. R. 2004 Intrusive gravity currents and internal gravity wave generation in stratified fluid. *J. Fluid Mech.* **514**, 355–383.

Forbes, L. K. & Hocking, G. C. 2007 An intrusion layer in stationary incompressible fluids. Part 2. Solitary waves. *Eur. J. Appl. Maths* **17**, 577–595.

Forbes, L. K., Hocking, G. C. & Farrow, D. E. 2006 An intrusion layer in stationary incompressible fluids. Part 1. Periodic waves. *Eur. J. Appl. Maths* **17**, 557–575.

Forbes, L. K., Chen, M. J. & Trenham, C. E. 2007 Computing unstable periodic waves at the interface of two inviscid fluids in uniform vertical flow. *J. Comput. Phys.* **221**, 269–287.

Fructus, D. & Grue, J. 2004 Fully nonlinear solitary waves in a layered stratified fluid. *J. Fluid Mech.* **505**, 323–347.

Lamb, H. 1932 *Hydrodynamics*. Dover.

Lewis, J. E., Lake, B. M. & Ko, D. R. S. 1974 On the interaction of internal waves and surface gravity waves. *J. Fluid Mech.* **63**, 773–800.

Mehta, A. P., Sutherland, B. R. & Kyba, P. J. 2002 Interfacial gravity currents. Part II. Wave excitation. *Phys. Fluids* **14**, 3558–3569.

Meiron, D. I. & Saffman, P. G. 1983 Overhanging interfacial gravity waves of large amplitude. *J. Fluid Mech.* **120**, 213–218.

Michallet, H. & Dias, F. 1999 Non-linear resonance between short and long waves. In *Proc. 9th Intl Offshore and Polar Engineering Conference*, pp. 193–198.

Părău, E. & Dias, F. 2001 Interfacial periodic waves of permanent form with free-surface boundary conditions. *J. Fluid Mech.* **437**, 325–336.

Phillips, O. M. 1969 *The Dynamics of the Upper Ocean*. Cambridge University Press.

Phillips, O. M. 1974 Non-linear dispersive waves. *Annu. Rev. Fluid Mech.* **6**, 93–108.

Pullin, D. I. & Grimshaw, R. H. J. 1983 Interfacial progressive gravity waves in a two-layer shear flow. *Phys. Fluids* **26**, 1731–1739.

Rusås, P.-O. & Grue, J. 2002 Solitary waves and conjugate flows in a three-layer fluid. *Eur. J. Mech.* B *Fluids* **21**, 185–206.

Saffman, P. G. & Yuen, H. C. 1982 Finite-amplitude interfacial waves in the presence of a current. *J. Fluid Mech.* **123**, 459–476.

Sutherland, B. R., Kyba, P. J. & Flynn, M. R. 2004 Intrusive gravity currents in two-layer fluids. *J. Fluid Mech.* **514**, 327–353.

Taylor, G. I. 1931 Effect of variation in density on the stability of superposed streams of fluid. *Proc. R. Soc. Lond.* A **82**, 499–523.

Timmermans, M.-L. E. & Pratt, L. J. 2005 Two-layer rotating exchange flow between two deep basins: Theory and application to the Strait of Gibraltar. *J. Phys. Ocean Ogr.* **35**, 1568–1592.

Turner, R. E. L. & Vanden-Broeck, J.-M. 1986 The limiting configuration of interfacial gravity waves. *Phys. Fluids* **29**, 372–375.

Vanden-Broeck, J.-M. & Turner, R. E. L. 1992 Long periodic internal waves. *Phys. Fluids* A **4**, 1929–1935.

Williams, M. J. M., Jenkins, A. & Determann, J. 1998 Physical controls on ocean circulation beneath ice shelves revealed by numerical models. In *Ocean, Ice, and Atmosphere: Interactions at the Antarctic Continental Margin* (ed. S. S. Jacobs & R. F. Weiss), pp. 285–299. American Geophysical Union.

Wilton, J. R. 1915 On ripples. *Phil. Mag.* **29**, 688–700.